Dinuclear Influence on the Mechanism, Reactivity, and Selectivity During Rh-Al Catalyzed Aryl Ether C-O Bond Reduction/Defunctionalization

Jugal Kumawat, Iran Daniela Macias, and Daniel H. Ess*

Department of Chemistry and Biochemistry, Brigham Young University, Provo 84604, Utah, United States

Keywords: Dinuclear, catalysis, heterodinuclear, bimetallic, aryl ether

Abstract

Dinuclear metal complexes with a direct metal-metal interaction have the potential for unique mechanisms, intermediates, and selectivity during catalysis. Here we report density functional theory (DFT) calculations that directly evaluate the influence of a dinuclear metal-metal interaction during aryl C−O bond reduction/defunctionalization with either hydrosilane or bis(pinacolato)diboron ($B_2(pin)_2$) reagents catalyzed by a heterodinuclear Rh−Al complex. Our calculations demonstrate the critical Rh−Al cooperative behavior necessary for aryl C−O bond activation and catalytic turnover. However, only the Rh metal center is involved in hydrosilane Si−H bond activation to generate a defunctionalized arene or B−B bond activation of $B_2(pin)_2$ to form an aryl bornic acid pinacol ester. The calculations also reveal an unanticipated very strong ligand-to-substrate steric effect that controls reduction site selectivity.

Introduction

Dinuclear complexes[1,2,3,4,5,6] are emerging as an alternative to classic mononuclear metal-ligand complexes for catalytic bond activation and functionalization reactions. This is because with two metal centers there is the potential for new mechanisms, intermediates, and selectivity.[7,8,9,10,11,12,13,14,15] These unique mechanisms and selectivity result from metal-metal interactions that may induce unique electronic effects (e.g. enhanced electrophilicity or nucleophilicity), nontraditional steric environments, and intermediate oxidation states. Therefore, our group is using density functional theory (DFT) calculations to understand the origin and influence of dinuclear effects on catalytic reactions, especially bond activation reactions.[16,17,18,19,20,21,22,23]

For heterodinuclear complexes with two transition metals or a transition metal and a main-group metal, there are now several classic examples of bond activation reactions. For example, Bergman showed that an Ir−Zr complexes with Cp ligands can stoichiometrically activate/break C−O, O−H, and N−H bonds through addition to both metal centers.[24,25] For transition metals combined with a main-group metal/atom, Braun showed that rhodium boryl (Rh−B)[26,27] and rhodium silyl (Rh−Si)[28,29] complexes can induce the activation of C−F bonds for catalytic functionalization of pentafluoropyridines and hexafluorobenzenes. As another example, Yamashita and Nozaki have reported tridentate pincer-type ligands for the activation of C−C bonds using Rh, Os, Ir and Pt metals with boryl donor PBP ligand complexes.[30,31,32,33,34] Similarly, Peters has demonstrated the hydrogenation of olefins through H_2 activation using Co/Ni−B complexes.[35] There are also heterodinuclear catalysts reported with Al to transition metal bonding. For example, Takaya and Iwasawa reported an Al−Pd complex that catalyzes CO_2 reduction.[36] Recently, Nakao developed a PAlP ligand framework mounted on Rh and Al metals and the heterodinuclear

complex showed catalytic C−O/C−C/C−F bond activation.[37,38,39] Sakaki's inspection of the metal-metal bonding of this complex suggests $Rh^{\delta-}-Al^{\delta+}$ bond polarization.[40,41]

Our focus in this work is a DFT-based evaluation of reactivity and selectivity for aryl ether C−O bond activation and reduction/defunctionalization catalyzed by the heterodinuclear Rh−Al complex **1A** reported by Nakao (Scheme 1a).[37] Aryl ether C−O bond cleavage is important because it is a model reaction for the more general process of converting oxygen-rich lignocellulosic biomass into more valuable deoxygenated fuels and chemicals.[42,43,44] Scheme 1a outlines the Rh−Al catalyzed selective C−O bond reduction of aryl ethers using either hydrosilane $H-Si(Me)(OSiMe_3)_2$ or bis(pinacolato)diboron ($B_2(pin)_2$) reductants. While mononuclear Ni catalysts, for example $Ni(COD)_2$-based catalysts with added phosphine ligands, are capable of inducing aryl ether C−O bond reduction[45] there is a dramatically different site selectivity of catalyst **1A** versus Ni-based catalysts. For example, Scheme 1b outlines several aryl ether reduction reactions where the Rh−Al catalyzed reaction selectively cleaves the methoxy group at the para position (relative to the pyridyl ring) while the Ni catalyst results in reduction at the ortho position. While Nakao proposed a plausible reaction mechanism for aryl ether C−O bond activation there was neither determination of alternative reaction mechanisms, the impact of the dinuclear effect, nor the detailed origins of the site selectivity. Also, it is likely that the Rh−Al catalyst operates in a very different mechanism compared to the mononuclear Ni catalysis, which for hydrosilane conditions Gómez-Bengoa and Martin proposed to involve a reactive Ni-silyl intermediate that induces dearomatization of the aryl ether followed by generation of a Ni-aryl intermediate.[45,46,47,48] There are also alternative mononuclear mechanisms proposed for related reaction conditions, such as cross-coupling or highly basic conditions.[49,50,51,52,53,54]

Therefore, here we report DFT calculations that comprehensively evaluated mechanisms, dinuclear cooperativity, and site selectivity for this Rh−Al catalyzed aryl ether C−O bond activation and reduction reaction. Our calculations demonstrate the critical Rh−Al cooperative behavior for C−O bond activation and catalytic turnover reaction steps but reveal that only the Rh metal center is involved in hydrosilane Si−H bond (or B−B bond) activation and reductive elimination of the arene product. The calculations also provide modeling of site selectivity induced by the Rh−Al catalyst, which shows a surprisingly strong ligand-to-substrate repulsive effect.

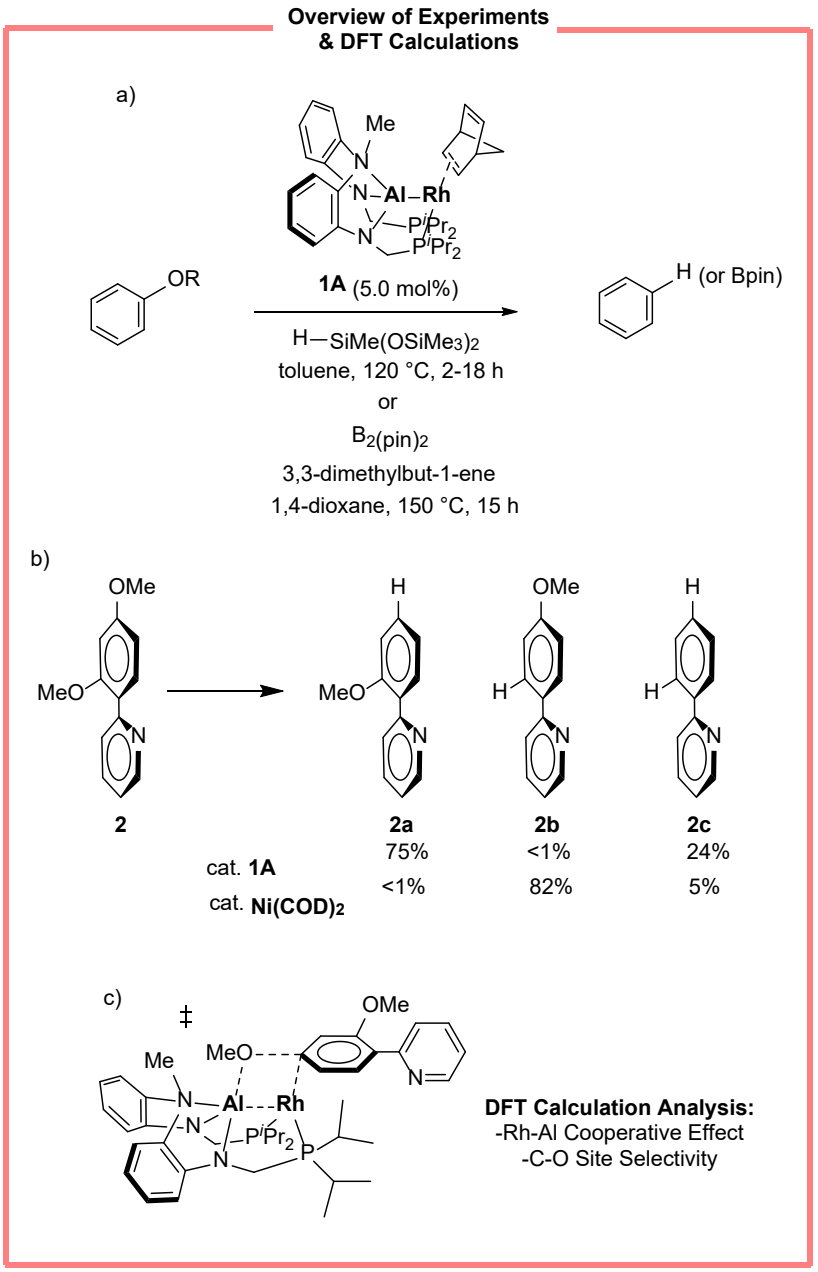

Scheme 1. a) Outline of experiments reported by Nakao for C–O aryl ether bond reduction/defunctionalization by the Rh–Al catalyst **1A**.[37] b) Comparison of heterodinuclear Rh–Al catalyzed site selectivity versus Ni catalyzed site selectivity. c) Outline of DFT calculations used in this work to examine the Rh–Al cooperative effect and aryl ether C-O bond reduction site selectivity.

Results and Discussions

Using the complete catalyst system in our calculations, we began by examining whether catalyst **1A** first coordinates and actives the hydrosilane Si−H bond (H−Si(Me)($OSiMe_3$)$_2$ was used in all calculations) or first coordinates and activates the aryl ether C−O bond of anisole. Gibbs energies refer to B2PLYP-D3(BJ)/def2-TZVPP//M06/def2-SVP[LANL2DZ] (see Computational Methods section for details). The top pathway in Figure 1 shows that loss of the bicyclic diene and coordination the silane to give structure **B**, which is 15.6 kcal/mol endergonic. After coordination of the Si−H bond there is a <1 kcal/mol barrier for complete cleavage of the bond to generate the Rh silyl hydride intermediate **B'** that is endergonic by 2.6 kcal/mol. While this Si−H bond activation pathway has a relatively low barrier, subsequent reactions from the Rh hydride intermediate **B'** have high barriers for reduction of the aryl ether C−O bond. For example, σ-Bond metathesis with the anisole C−O bond has a transition-state barrier of 86.5 kcal/mol (**TS$_C$**) and hydride donation to the aryl ring (**TS$_{C'}$**) of anisole has a barrier of 77.1 kcal/mol. This suggests that coordination and activation of the Si−H bond is overall reversible and likely occurs off cycle.

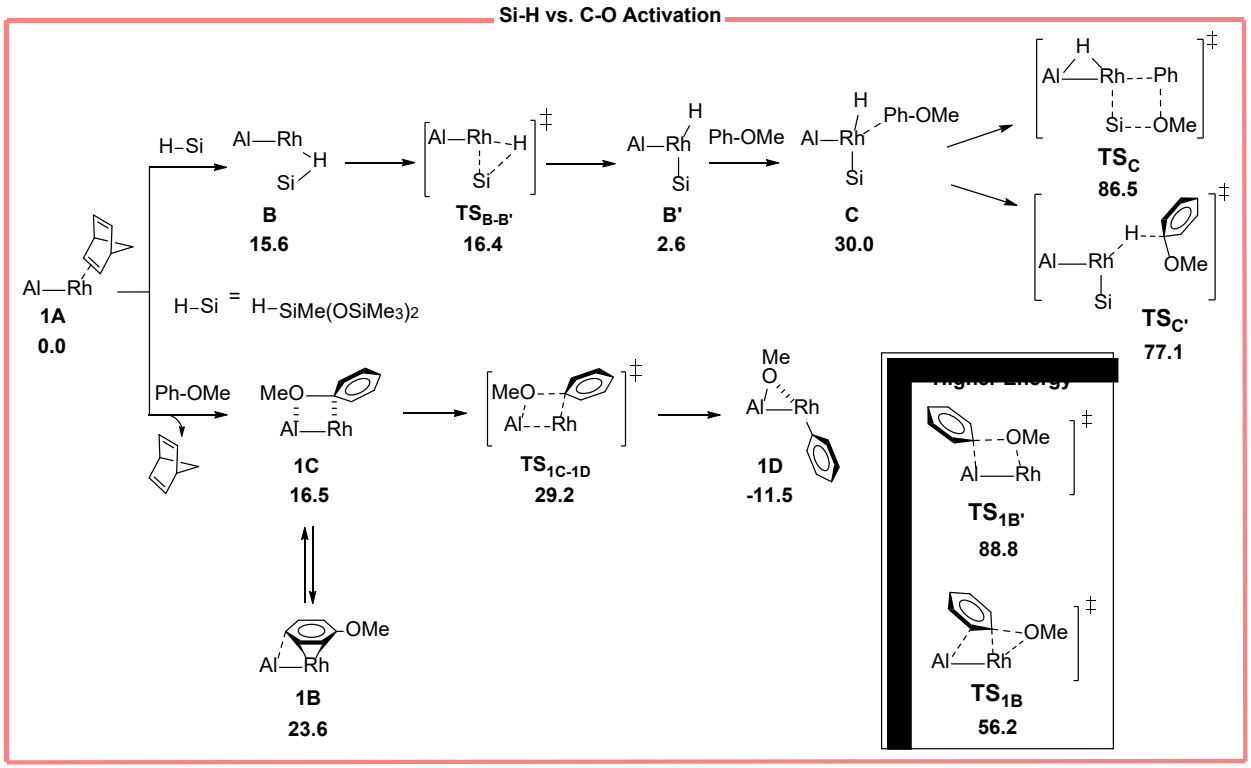

Figure 1. Outline of hydrosilane Si−H bond and aryl ether C−O bond coordination and cleavage pathways. Insert shows higher energy C−O bond cleavage transition states. The catalyst **1A** is abbreviated in the scheme as Al−Rh without ligands for clarity. B2PLYP-D3(BJ)/def2-TZVPP//M06/def2-SVP[LANL2DZ] Gibbs energies reported in kcal/mol.

The lower pathway in Figure 1 outlines aryl ether C−O bond activation. Anisole can approach either to form a π-complex with the Rh metal center **1B** (23.6 kcal/mol) or coordinate through the C−O σ bond **1C** (16.5 kcal/mol). In **1B** there is no significant π-coordination of the anisole with the Al center, likely due to the steric influence of N-Me ligand framework. From these weak coordination structures, we located three different anisole C−O bond activation transition states. **TS$_{1C-1D}$** (Figures 1 and 2) involves addition of the C−O bond across the Rh and Al metal centers with a Gibbs transition-state barrier of 29.2 kcal/mol. This transition state leads directly to intermediate **1D** that was experimentally characterized by Nakao,[37] which is consistent with it being exergonic by 11.5 kcal/mol.

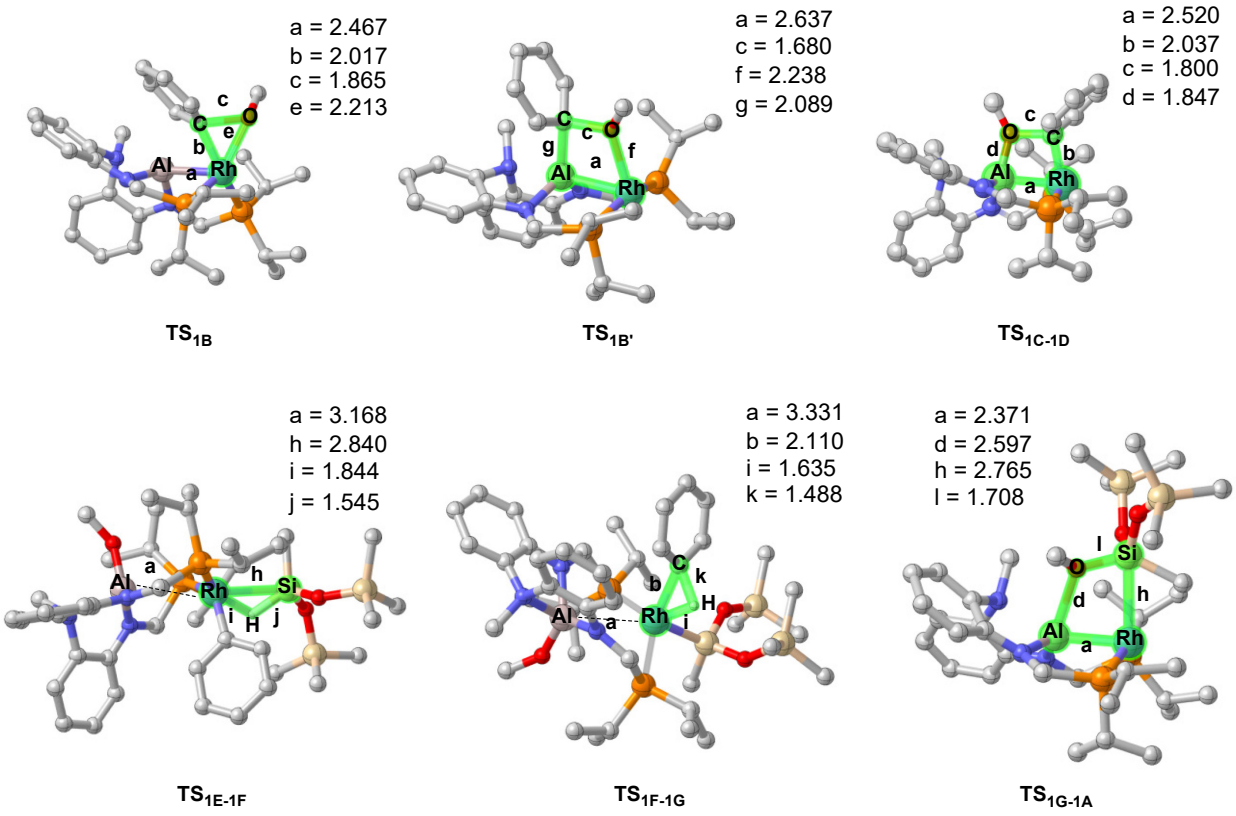

Figure 2. 3D representations of optimized transition-state structures. All distances are reported in Å.

Previous natural bond orbital analysis of **1A** indicated a polar covalent Rh−Al bond with a Rh metal center oxidation state between +1 and 0.[40] Our own molecular orbital component analysis (see Supporting Information (SI) for details) also suggests the Rh−Al bond in **1A** can be described as a polar covalent bond with Rh having an approximate oxidation state of 0. We also analyzed the molecular orbitals of intermediate **1D**. This analysis indicates that the Rh metal center has an oxidation state of +1 because the new Rh−Ph bond ($Rh^{\delta+}$–$C^{\delta-}$ polarization) is formed using a nonbonding d-electron pair, the new Al−OMe bond is formed using the Al p orbital, and the Rh−Al electron pair becomes highly shifted to the Rh metal center (see SI). The shift from a polar covalent to dative Rh−Al interaction is consistent with the distance increasing by ~0.2 Å.

To directly evaluate the energy influence of the Al metal center during C−O bond activation we also located transition states **TS_{1B}** and **$TS_{1B'}$**, which are shown in the insert of Figure 1. **TS_{1B}** is the three-centered oxidative addition transition state that results in a Rh phenyl methoxide intermediate. In this transition state there is only a very weak interaction between the Al center the anisole aromatic ring. The Gibbs barrier for this Rh centered oxidative addition is 56.2 kcal/mol, which is relatively high given the strong σ-donating capacity of the Al to the Rh metal center. **$TS_{1B'}$** was located where the anisole C−O bond addition across the Rh−Al bond results in a Rh−OMe/Al−Ph intermediate, and due to the reversal of inherent bond polarity has an extremely high barrier of 88.8 kcal/mol.

From **1D**, either H−Si(Me)$(OSiMe_3)_2$ (H−Si in Figure 3) or $B_2(pin)_2$ can react with the Rh−Ph bond. The right-hand energy surface in Figure 3 shows the energy profile of the lowest energy pathway identified for reaction with the hydrosilane Si−H bond and the left-hand energy surface is the pathway for reaction with $B_2(pin)_2$. Coordination of these reductants to **1D** and formation of **1E** and **1'E** are endergonic by 5.6 and 15.6 kcal/mol, respectively. Like the aryl ether C−O bond activation step, we initially thought that both metal centers would be involved with Si−H or B−B bond activation reaction steps. However, for both substrates we only located transition states where bond activation occurs at the Rh metal center (three-membered transition states), **$TS_{1E\text{-}1F}$** and **$TS_{1'E\text{-}1'F}$** (Figures 2 and 3), which lead to intermediates **1F** and **1'F**. Because of the newly formed Rh−H/Rh−Si bonds or Rh−B bonds intermediates **1F** and **1'F** have a completely severed Rh−Al dative interaction and these intermediates are probably best described with Rh having respectively 0 and +1 oxidation states (see SI for discussion and display of molecular orbitals).[55] The Gibbs barriers from **1D** to these transition states are 41.3 for the hydrosilane and 36.4 kcal/mol for $B_2(pin)_2$. From these endergonic **1F** and **1'F** intermediates

subsequent three-membered reductive coupling transition states to form benzene and PhB(pin) products through $\mathbf{TS_{1F\text{-}1G}}$ and $\mathbf{TS_{1'F\text{-}1'G}}$ have small barriers of only ~5-6 kcal/mol.

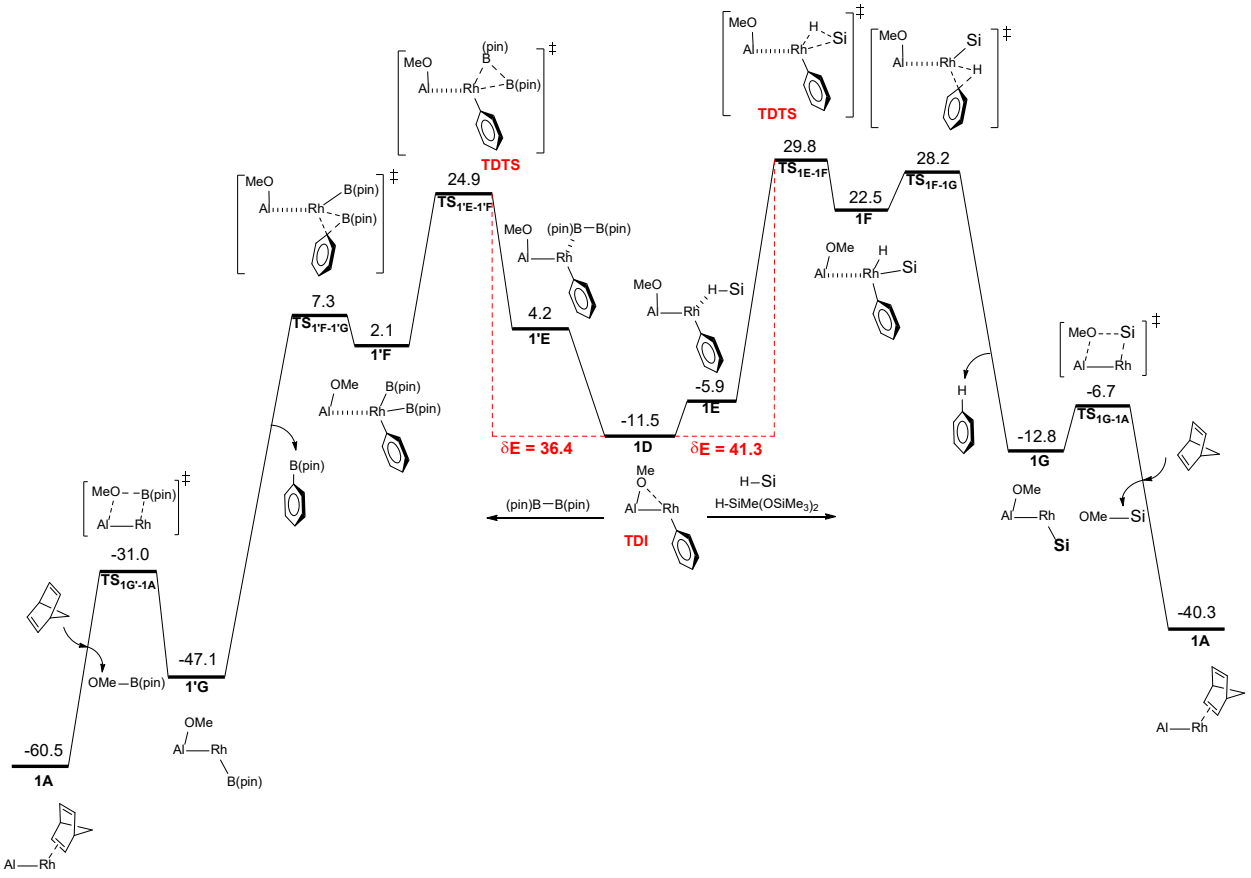

Figure 3. Gibbs energy profiles for anisole reduction/defunctionalization with H−Si(Me)$(OSiMe_3)_2$ and $B_2(pin)_2$ catalyzed by **1A**. B2PLYP-D3(BJ)/def2-TZVPP//M06/def2-SVP[LANL2DZ] Gibbs energies reported in kcal/mol.

To complete the catalytic cycle and reform the Rh−Al bond, from **1G** and **1'G** intermediates we located four-centered transition states $\mathbf{TS_{1G\text{-}1A}}$ and $\mathbf{TS_{1'G\text{-}1'A}}$. The Gibbs barriers for these transition states are 6.1 and 16.1 kcal/mol, respectively. Both reaction steps are highly exergonic due to the formation of the Si−O and B−O bonds. We have also examined the possibility that **1G** and **1'G** intermediates react with a second anisole. For example, the Rh−Si bond could directly undergo a σ-bond metathesis with anisole. However, the barriers for this type of process are >60 kcal/mol and unlikely.

With a complete catalytic cycle outlined in Figures 1 and 3 it was possible to determine which reaction step(s) control the catalytic turnover rate. We used the catalytic energy span model of Kozuch and Shaik,[56,57] which is related to Campell's degree of rate control idea,[58] and this identified intermediate **1D** as the dominant resting state and **TS$_{1E-1F}$**/**TS$_{1'E-1'F}$** as the dominant catalytic rate controlling transition state, which are both after the C−O bond activation step. This is consistent with the experimental observation of **1D**. However, depending on the density functional method used **TS$_{1E-1F}$** and **TS$_{1F-1G}$** have very similar energies and so both can contribute to controlling the catalytic rate, which is the case with B2PLYP-D3(BJ). The energetic span δE (see Figure 3) between **1D** and **TS$_{1E-1F}$** and **1D** and **TS$_{1'E-1'F}$** are 41.3 and 36.4 kcal/mol for reaction with the hydrosilane and $B_2(pin)_2$. Other density functional methods gave very similar energy span values. For example, PWPB95-D3(BJ)/def2-TZVPP//M06/def2-SVP[LANL2DZ] gave an energy span of 41.6 kcal/mol for reaction with the hydrosilane. These moderately large energy spans showcase the relatively slow catalysis and are consistent with the 120-150 °C temperatures required to obtain significant conversion.

Based on the mechanism of C−O bond reduction outlined in Figures 1 and 3, we examined the kinetic reduction site selectivity for the anisole derivative **2** shown in Scheme 1 and anisole derivatives **3** and **4** shown in Schemes 2a and 2b. From the interpretation of the energy landscape, for reduction using $B_2(pin)_2$ site selectivity is set during the C−O bond activation/cleavage step since it is irreversible, which is demonstrated by **TS$_{1E-1F}$** having a lower forward barrier than the reverse barrier back to **TS$_{1C-1D}$** from intermediate **1D** (compare Figures 1 and 3). For reduction using H−Si(Me)$(OSiMe_3)_2$, it is possible that C−O bond cleavage might be partially reversible since the forward and reverse barriers emanating from intermediate **1D** are very similar. Therefore, we have examined selectivity for both C−O and Si−H bond cleavage reaction steps.

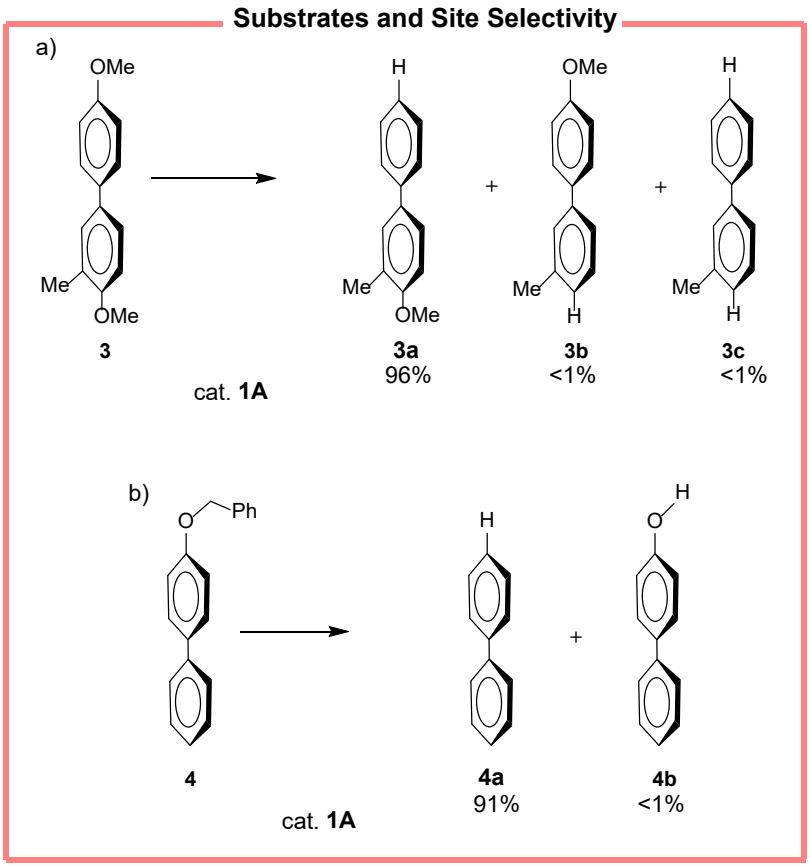

Scheme 2. Experimental site selectivity reported by Nakao with Rh−Al catalyst **1A** (shown in Scheme 1) for a) substrate **3** and b) substrate **4**.[37]

For the pyridyl anisole **2**, Figure 4 shows the full energy landscape for H−Si(Me)$(OSiMe_3)_2$ reaction with the two different C−O bonds. For the C−O bond activation step, $\mathbf{TS_{2C\text{-}2D}}$ with activation of the C−O bond para to the pyridyl ring is lower in Gibbs energy than $\mathbf{TS_{2'C\text{-}2'D}}$ (ortho position) by 6.9 kcal/mol (see Figure 5 for 3D images). Surprisingly, the relative stabilities of the resulting **2D** and **2'D** intermediates from C−O bond cleavage are inverted compared to their transition states. Importantly, regardless of the reversibility of the C−O bond activation there is also a large kinetic preference for $\mathbf{TS_{2E\text{-}2F}}$ versus $\mathbf{TS_{2'E\text{-}2'F}}$ (Si−H activation step). The 6.9 kcal/mol and 8.6 kcal/mol (for $\mathbf{TS_{2E\text{-}2F}}$/$\mathbf{TS_{2'E\text{-}2'F}}$) energy differences for these reaction steps are fully consistent with experiments showing products for a single reduction/defunctionalization at the para

position. When double reduction occurs, it would first proceed through reduction at the para position followed by a second catalytic cycle with transition states and intermediates similar to those shown in Figure 3 for a mono-substituted aryl ring.

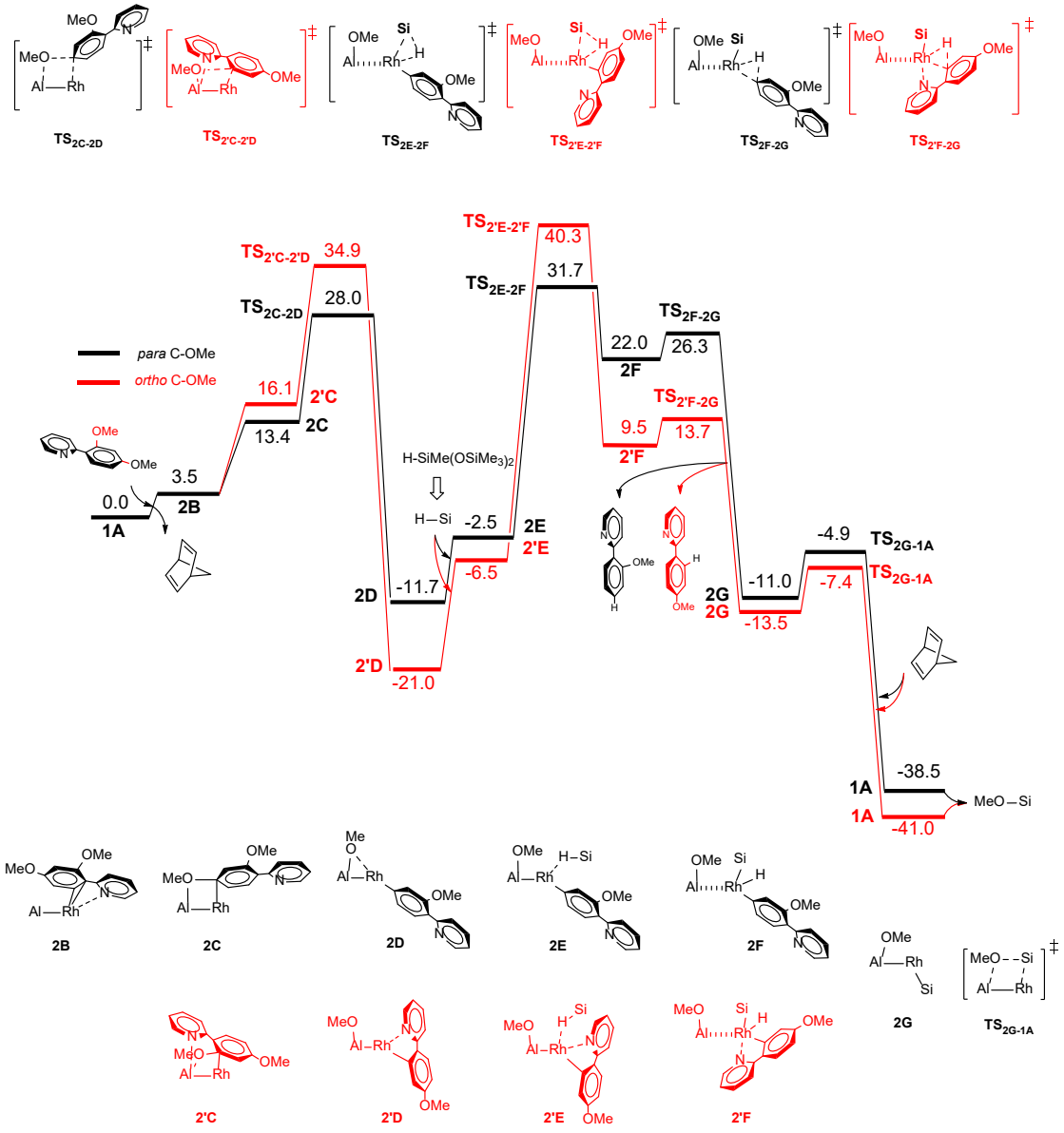

Figure 4. Gibbs energy profiles for C−O bond reduction site selectivity of substrate **2** with H−Si(Me)$(OSiMe_3)_2$. B2PLYP-D3(BJ)/def2-TZVPP//M06/def2-SVP[LANL2DZ] Gibbs energies reported in kcal/mol.

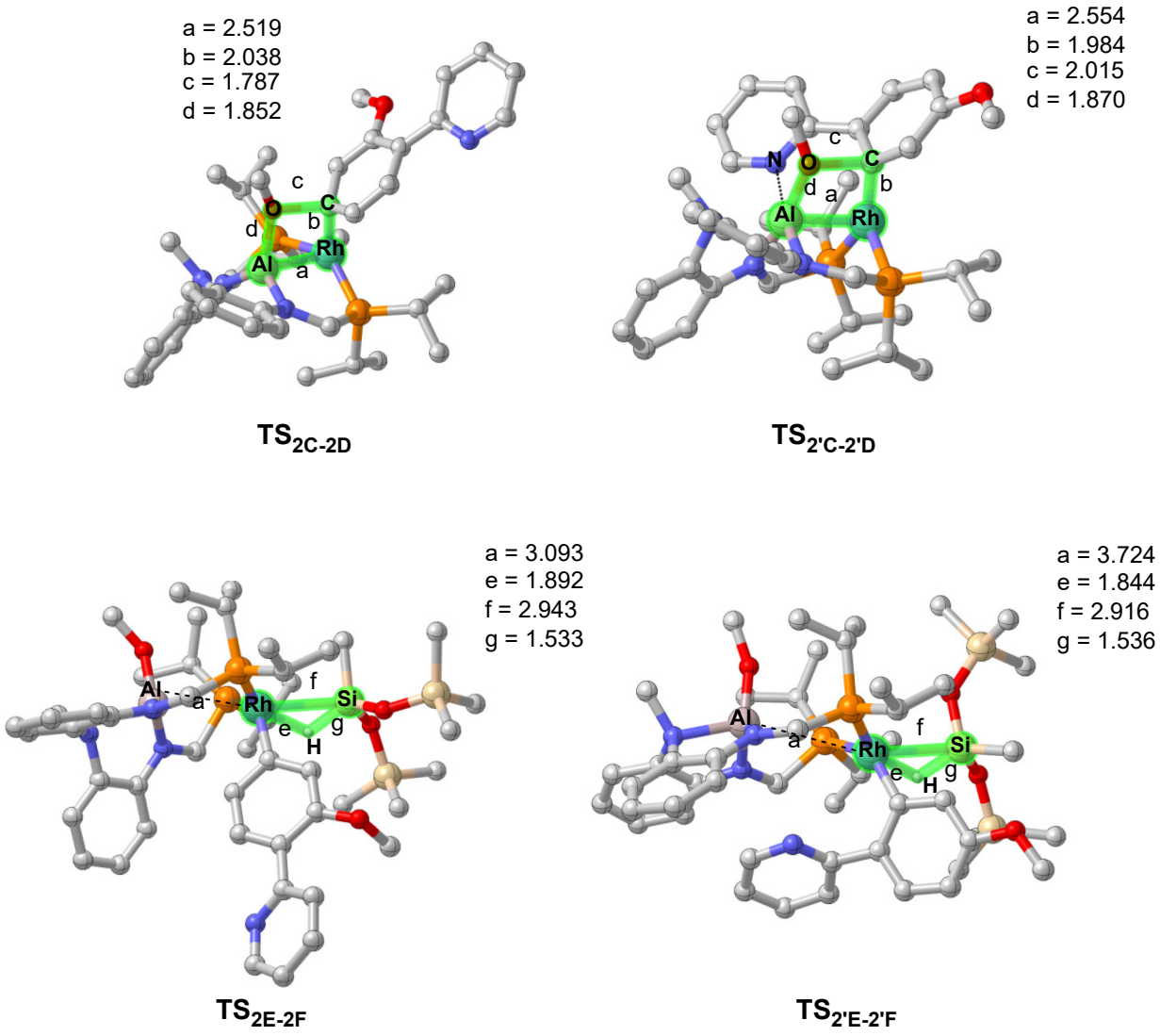

Figure 5. 3D depictions of transition-state structures controlling C−O bond reduction/defunctionalization site selectivity. All distances are reported in Å.

We also calculated the site selectivity for substrates **3** and **4**. The Gibbs energy profiles for activation and reduction of the C−O bonds for substrates **3** and **4** are provided in the SI. For **3**, there is a 2.1 kcal/mol lower transition state for C−O bond cleavage through $\mathbf{TS_{3C\text{-}3D}}$ compared to $\mathbf{TS_{3'C\text{-}3'D}}$. There is also >10 kcal/mol preference for reaction at this position through $\mathbf{TS_{3E\text{-}3F}}$. Like substrate **2**, the relative transition states show high selectivity for the para position.

With the ability of the DFT calculations to model the reduction site selectivity, we wanted to change the ligand scaffold and re-calculate relative barrier heights to determine the origin of selectivity. We were especially intrigued by the origin of selectivity for substrate **2** because in the higher energy C−O cleavage transition state $\mathbf{TS_{2'C\text{-}2'D}}$ there is a unique pyridyl-Al coordination interaction while for $\mathbf{TS_{2C\text{-}2D}}$ this interaction is not present (compare structures in Figure 5). We were also intrigued in how significantly different key distances are in structures $\mathbf{TS_{2C\text{-}2D}}$ and $\mathbf{TS_{2'C\text{-}2'D}}$. For example, the breaking C−O bond length in $\mathbf{TS_{2C\text{-}2D}}$ is 1.79 Å while it is much more elongated at 2.02 Å in $\mathbf{TS_{2'C\text{-}2'D}}$.

Figure 6 outlines the several modifications to catalyst **1A** that we used to analyze the origin of selectivity. We began by disconnecting the pyridyl-Al interaction in $\mathbf{TS_{2'C\text{-}2'D}}$ with rotation of the pyridyl ring so that a C−H bond rather than the nitrogen atom was directed towards the Al metal center. We initially assumed that this donor interaction decreased the ability of the Al center to act as a strong Lewis acid in breaking the C−O bond. However, re-optimization of this structure showed that energy of $\mathbf{TS_{2'C\text{-}2'D}}$ increased by 4.3 kcal/mol to give a relative transition-state energy of 11.1 kcal/mol, which means this interaction overall stabilizes the transition state and therefore the pyridyl-Al interaction does not determine site selectivity. Similarly, change of the pyridyl group to a phenyl group in both transition states gave a $\Delta\Delta G^{\ddagger}$ value of 10.5 kcal/mol. The results of the phenyl substitution then prompted us to change the pyridyl ring to a methyl group, which we assumed would significantly decrease the $\Delta\Delta G^{\ddagger}$ value and calculated selectivity. To our surprise the energy difference was 9.4 kcal/mol, which is larger than the difference between the original transition-state energies.

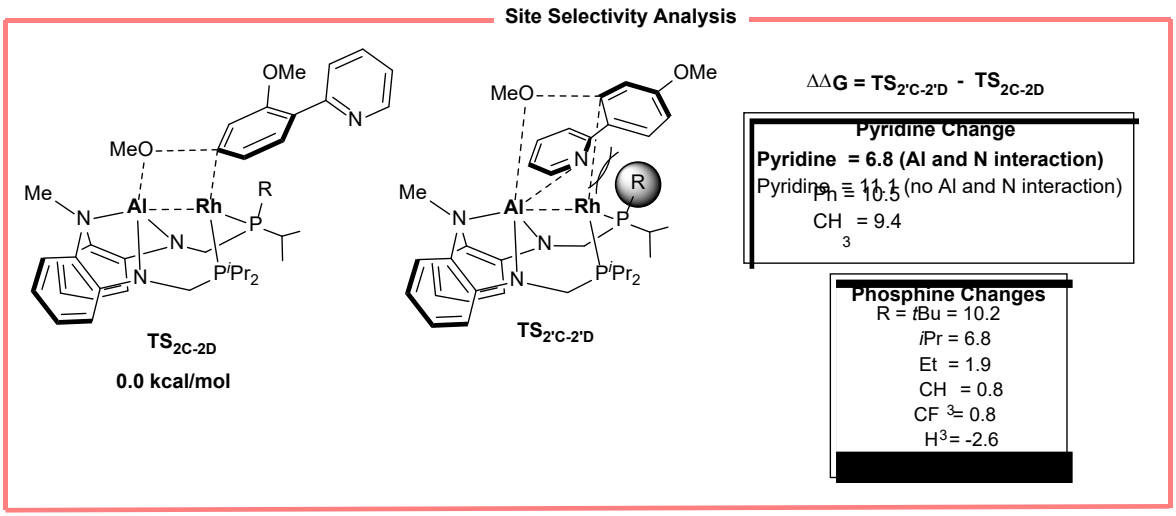

Figure 6. Analysis of selectivity for aryl ether substrate **2**. B2PLYP-D3(BJ)/def2-TZVPP//M06/def2-SVP[LANL2DZ] Gibbs energies reported in kcal/mol.

With the surprise that a the relatively small methyl group substituent can result in a relatively large energy difference between structures **TS$_{2C-2D}$** and **TS$_{2'C-2'D}$** this suggested that the transition state requires a conformation where this group is greatly impinged by the phosphine ligand. Indeed, inspection of the 3D structures in Figure 5 show that one of the phosphine isopropyl groups is oriented directly towards the pyridyl ring. However, the distance between the isopropyl hydrogen and the pyridyl ring is ~2.5 Å and it was unclear if this interaction distance is overall repulsive or overall stabilizing through dispersive type interactions. Therefore, we replaced this single isopropyl group with *tert*-butyl, ethyl, methyl, trifluoromethyl, and hydrogen. Indicative of a repulsive, steric type of interaction the *tert*-butyl resulted in an increased $\Delta\Delta G^{\ddagger}$ value while for ethyl and methyl the $\Delta\Delta G^{\ddagger}$ value decreased to 1.9 and 0.8 kcal/mol, respectively. Interestingly, the relative energies of these transition states can be inverted. With trifluoromethyl the transition states have almost equal energy and with hydrogen **TS$_{2'C-2'D}$** is lower in energy than **TS$_{2C-2D}$**. Overall, this indicates that with re-design of the phosphine section of the ligand there is the possibility to significantly alter site selectivity and potentially favor a different position.

Conclusion

Our DFT calculations provided an in-depth set of reaction steps for aryl C−O bond reduction/defunctionalization catalyzed the heterodinuclear Rh−Al complex **1A**. The first reaction step is aryl ether C−O bond activation rather than hydrosilane Si−H bond activation, which may be a reversible off cycle reaction step. The exothermic Al−OMe/Rh−Ar intermediate and subsequent rate controlling hydrosilane Si−H bond activation step is consistent with the experimental observation of this intermediate. Importantly, the Rh−Al heterodinuclear metal-metal interaction is critical for C−O bond activation and catalytic turnover generating methoxy silane but hydrosilane Si−H bond activation and arene reductive elimination (aryl-BPin reductive elimination) occurs only at the Rh metal center. This mechanism is very different than the catalytic mononuclear Ni mechanism that has been proposed for the combination of Ni with phosphine ligand.[45] In the case of mononuclear Ni catalysis it was proposed that a Ni-silyl intermediate facilitates a nucleophilic aromatic addition/σ-bond metathesis pathway to give a Ni-aryl intermediate. For reduction site selectivity, we initially assumed that the pyridyl group coordination to the Al metal center in the transition state greatly influenced selectivity. However, modifications of the catalyst ligand followed by re-calculation of the key transition states showed a strong repulsive steric effect driving selectivity.

Computational Methods

Optimization of intermediate and transition-state structures was completed using Gaussian 16 with the default ultrafine integration grid.[59] The M06[60] hybrid density functional was used with the Los Alamos ECP[61] (LANL2DZ for Rh) and def2-SVP basis sets.[62] All of the stationary points were characterized either as a minimum or a first-order saddle point using vibrational frequency

analysis. Intrinsic reaction coordinate (IRC) calculations were also performed to verify proposed potential-energy surface connections.[63] During both optimization and single point calculations solvent stabilization was incorporated using the conductor-like polarizable continuum model (CPCM) method for toluene and 1,4-Dioxane.[64] Single-point energies were calculated using M06/def2-TZVPD and B3LYP-D3(BJ)/def2-TZVPD in Gaussian and the double hybrid functional B2PLYP-D3(BJ)/def2-TZVPP in ORCA.[65] For select structures, single-point energies were also calculated using PWPB95-D3(BJ)/def2-TZVPP in ORCA. Analysis of turnover-determining reaction intermediates (TDIs) and transition states (TDTSs) was done using Shaik and Kozuch's energy span model.[56,57]

Supporting Information

Additional computational details, Rh−Al bond analysis, xyz structures, and energies.

Author Information

***Daniel H. Ess** – *Department of Chemistry and Biochemistry, Brigham Young University, Provo, Utah 84604, United States*; Email: dhe@chem.byu.edu

Acknowledgements

The authors thank Brigham Young University and the Fulton Supercomputing Lab for computational resources. This work was supported by the US National Science Foundation with award CHE-2153215. A preliminary report of this work was deposited on ChemRxiv: https://chemrxiv.org/engage/chemrxiv/article-details/64246671647e3dca99b59ed3

References

1. Sinfelt, J. H. Bimetallic Catalysts: Discoveries, Concepts and Applications; John Wiley and Sons: New York, 1983, XI + 164 pp.

2. Bullock, R. M.; Casey, C. P. Heterobimetallic Compounds Linked by Heterodifunctional Ligands. *Acc. Chem. Res.* **1987**, *20*, 167−173.

3. Stephan, D. W. Early-late Heterobimetallics. *Coord. Chem. Rev.* **1989**, *95*, 41−107.

4. Beuken, E. K. van den; Feringa, B. L. Bimetallic Catalysis by Late Transition Metal Complexes. *Tetrahedron* **1998**, *54*, 12985−13011.

5. Wheatley, N.; Kalck, P. Structure and Reactivity of Early-Late Heterobimetallic Complexes. *Chem. Rev.* **1999**, *99*, 3379−3419.

6. Gade, L. H. Highly Polar Metal-Metal Bonds in "Early-Late" Heterobimetallic Complexes. *Angew. Chem. Int. Ed.* **2000**, *39*, 2658−2678.

7. Thomas, C. M. Metal-metal Multiple Bonds in Early/Late Heterobimetallic Complexes: Applications Toward Small Molecule Activation and Catalysis. *Comments on Inorganic Chemistry* **2011**, *32*, 14−38.

8. Cooper, B. G.; Napoline, J. W.; Thomas, C. M. Catalytic Applications of Early/Late Heterobimetallic Complexes *Catal. Rev.* **2012**, *54*, 1−40.

9. Mankad, N. P. Selectivity Effects in Bimetallic Catalysis. *Chem. Eur. J.* **2016**, *22*, 5822-5829.

10. Powers, D. C.; Ritter, T. Bimetallic Redox Synergy in Oxidative Palladium Catalysis. *Acc. Chem. Res.* **2012**, *45*, 840−850.

11. Berry, J. F. Metal-Metal Multiple Bonded Intermediates in Catalysis. *J. Chem. Sci.* **2015**, *127*, 209−214.

12. Buchwalter, P.; Rose, J.; Braunstein, P. Multimetallic Catalysis Based on Heterometallic Complexes and Clusters. *Chem. Rev.* **2015**, *115*, 28−126.

13. Ed. Kalck, P.; Homo- and Heterobimetallic Complexes in Catalysis: Cooperative Catalysis Topics in Organometallic Chemistry, Vol. 59, **2016**, Springer.

14. Powers, I. G.; Uyeda, C. Metal-Metal Bonds in Catalysis. *ACS Catal.* **2017**, 7, 936−958.

15. Pye, D. R.; Mankad, N. P. Bimetallic catalysis for C-C and C-X coupling reactions. *Chem. Sci.* **2017**, *8*, 1705−1718.

16. Walker, W. K.; Kay, B. M.; Michaelis, S. A.; Anderson, D. L.; Smith, S. J.; Ess, D. H.; Michaelis, D. J. Origin of Fast Catalysis in Allylic Amination Reactions Catalyzed by Pd-Ti Heterobimetallic Complexes. *J. Am. Chem. Soc.* **2015**, *137*, 7371−7378.

17. Zhang, Y.; Roberts, S. P.; Bergman, R. G.; Ess, D. H. Mechanism and Catalytic Impact of Ir-Ta Heterobimetallic and Ir-P Transition Metal/Main Group Interactions on Alkene Hydrogenation. *ACS Catal.* **2015**, *5*, 1840−1849.

18. Kwon, D-H.; Proctor, M.; Mendoza, S.; Uyeda, C.; Ess, D. H. Catalytic Dinuclear Nickel Spin Crossover Mechanism and Selectivity for Alkyne Cyclotrimerization. *ACS Catal.* **2017**, 7, 4796−4804.

19. Coombs, J.; Perry, D.; Kwon, D-H.; Thomas, C. M.; Ess, D. H. Why Two Metals Are Better Than One for Cobalt Phosphinoamide Catalyzed Kumada Coupling. *Organometallics* **2018**, *37*, 4195−4203.

20. Zhang, Y.; Karunananda, M.; Williams, W.; Clark, K.; Mankad, N.; Ess, D. H. Dynamically Bifurcating Hydride Transfer Mechanism and Origin of Inverse Kinetic Isotope Effect for Heterodinuclear AgRu-Catalyzed Alkyne Semi-Hydrogenation. *ACS Catal.* **2019**, *9*, 2657−2663.

21. Ence, C. C.; Martinez, E. E.; Himes, S. R.; Nazari, S. H.; Moreno, M. R.; Matu, M. F.; Larsen, S. G.; Gassaway, K. J.; Valdivia-Berroeta, G. A.; Smith, S. J.; Ess, D. H.; Michaelis, D. J. Experiment and Theory of Bimetallic Pd-Catalyzed α-Arylation and Annulation for Naphthalene Synthesis. *ACS Catal.* **2021**, *11*, 10394−10404.

22. Steiman, T. J.; Kalab, A. E.; Coombs, J. C.; Kirkland, J. K.; Torres, H.; Ess, D. H.; Uyeda, C. Dinickel-Catalyzed Vinylidene−Alkene Cyclization Reactions. *ACS Catal.* **2021**, *11*, 14408−14416.

23. Kong, F.; Chen, S.; Chen, J.; Liu, C.; Zhu, W.; Dickie, D. A.; Ess, D. H. Zhang, S.; Gunnoe, T. B. Cu(II) Carboxylate Arene C–H Functionalization: Tuning for Non-Radical Pathways. *Sci. Adv.* **2022**, *8*, eadd 1594.

24. Baranger, A. M.; Bergman, R. G. Cooperative Reactivity in the Interactions of X-H Bonds with a Zirconium-Iridium Bridging Imido Complex. *J. Am. Chem. Soc.* **1994**, *116*, 3822−3835.

25. Hanna, T. A.; Baranger, A. M.; Bergman, R. G. Reaction of Carbon Dioxide and Heterocumulenes with an Unsymmetrical Metal-Metal Bond. Direct Addition of Carbon Dioxide across a Zirconium-Iridium Bond and Stoichiometric Reduction of Carbon Dioxide to Formate. *J. Am. Chem. Soc.* **1995**, *117*, 11363−11364.

26. Braun, T.; Ahijado Salomon, M.; Altenhöner, K.; Teltewskoi, M.; Hinze, S. C-F Activation at Rhodium Boryl Complexes: Formation of 2-Fluoroalkyl-1,3,2-Dioxaborolanes by Catalytic Functionalization of Hexafluoropropene. *Angew. Chem. Int. Ed.* **2009**, *48*, 1818−1822.

27 Teltewskoi, M.; Panetier, J. A.; Macgregor, S. A.; Braun, T. A Highly Reactive Rhodium(I)–Boryl Complex as a Useful Tool for C-H Bond Activation and Catalytic C-F Bond Borylation. *Angew. Chem. Int. Ed.* **2010**, *49*, 3947−3951.

28. Raza, A. L.; Panetier, J. A.; Teltewskoi, M.; Macgregor, S. A.; Braun, T. Rhodium(I) Silyl Complexes for C–F Bond Activation Reactions of Aromatic Compounds: Experimental and Computational Studies. *Organometallics* **2013**, *32*, 3795−3807.

29. Raza, A. L.; Braun, T. Consecutive C–F bond activation and C–F bond formation of heteroaromatics at rhodium: the peculiar role of $FSi(OEt)_3$. *Chem. Sci.* **2015**, *6*, 4255−4260.

30. Segawa, Y.; Yamashita, M.; Nozaki, K. Syntheses of PBP Pincer Iridium Complexes: A Supporting Boryl Ligand. *J. Am. Chem. Soc.* **2009**, *131*, 9201−9203.

31. Segawa, Y.; Yamashita, M.; Nozaki, K. Diphenylphosphino- or Dicyclohexylphosphino-Tethered Boryl Pincer Ligands: Syntheses of PBP Iridium(III) Complexes and Their Conversion to Iridium−Ethylene Complexes. *Organometallics* **2009**, *28*, 6234−6242.

32. Makoto, Y. Creation of Nucleophilic Boryl Anions and Their Properties. *Bull. Chem. Soc. Jpn.* **2011**, *84*, 983−999.

33. Hasegawa, M.; Segawa, Y.; Yamashita, M.; Nozaki, K. Isolation of a PBP-Pincer Rhodium Complex Stabilized by an Intermolecular C-H σ Coordination as the Fourth Ligand. *Angew. Chem. Int. Ed.* **2012**, *51*, 6956−6960.

34. Yamashita, M. The Organometallic Chemistry of Boron-Containing Pincer Ligands based on Diazaboroles and Carboranes. *Bull. Chem. Soc. Jpn.* **2016**, *89*, 269−281.

35. Lin, T.-P.; Peters, J. C. Boryl–Metal Bonds Facilitate Cobalt/Nickel-Catalyzed Olefin Hydrogenation. *J. Am. Chem. Soc.* **2014**, *136*, 13672−13683.

36. Takaya, J.; Iwasawa, N. Synthesis, Structure, and Catalysis of Palladium Complexes Bearing a Group 13 Metalloligand: Remarkable Effect of an Aluminum-Metalloligand in Hydrosilylation of CO2. *J. Am. Chem. Soc.* **2017**, *139*, 6074−6077.

37. Seki, R.; Hara, N.; Saito, T.; Nakao, Y. Selective C–O Bond Reduction and Borylation of Aryl Ethers Catalyzed by a Rhodium–Aluminum Heterobimetallic Complex. *J. Am. Chem. Soc.* **2021**, *143*, 6388−6394.

38. Hara, N.; Saito, T.; Semba, K.; Kuriakose, N.; Zheng, H.; Sakaki, S.; Nakao, Y. Rhodium Complexes Bearing PAlP Pincer Ligands. *J. Am. Chem. Soc.* **2018**, *140*, 7070−7073.

39. Fujii, I.; Semba, K.; Li, Q.-Z.; Sakaki, S.; Nakao, Y. Magnesiation of Aryl Fluorides Catalyzed by a Rhodium–Aluminum Complex. *J. Am. Chem. Soc.* **2020**, *142*, 11647−11652.

40. Kuriakose, N.; Zheng, J.-J.; Saito, T.; Hara, N.; Nakao, Y.; Sakaki, S. Characterization of Rh–Al Bond in Rh(PAlP) (PAlP = Pincer-type Diphosphino-Aluminyl Ligand) in Comparison with Rh(L)(PMe3)2 (L = $AlMe_2$, $Al(NMe_2)_2$, BR_2, SiR_3, CH_3, Cl, or OCH_3): Theoretical Insight. *Inorg. Chem.* **2019**, *58*, 4894−4906.

41. Li, Q.-Z.; Hara, N.; Nakao, Y.; Sakaki, S. Coordination Flexibility of the Rh(PXP) Complex to NH_3, CO, and C_2H_4 (PXP = Diphosphine-Based Pincer Ligand; X = B, Al, and Ga): Theoretical Insight. *Inorg. Chem.* **2020**, *59*, 15862-15876.

42. Sergeev, A. G.; J. F. Hartwig, J. F. Selective, Nickel-Catalyzed Hydrogenolysis of Aryl Ethers. *Science* **2011**, *332*, 439−443.

43. Sergeev, A. G.; Webb, J. D.; Hartwig, J. F. A Heterogeneous Nickel Catalyst for the Hydrogenolysis of Aryl Ethers without Arene Hydrogenation. *J. Am. Chem. Soc.* **2012**, 134, 20226−20229.

44. Saper, N. I.; Hartwig, J. F. Mechanistic Investigations of the Hydrogenolysis of Diaryl Ethers Catalyzed by Nickel Complexes of N-Heterocyclic Carbene Ligands. *J. Am. Chem. Soc.* **2017**, *139*, 17667−17676.

45. Cornella, J.; Gómez-Bengoa, E.; Martin, R. Combined Experimental and Theoretical Study on the Reductive Cleavage of Inert C−O Bonds with Silanes: Ruling out a Classical Ni(0)/Ni(II) Catalytic Couple and Evidence for Ni(I) Intermediates. *J. Am. Chem. Soc.* **2013**, *135*, 1997−2009.

46. Corneall, J.; Zarate, C.; Martin, R. Metal-catalyzed activation of ethers via C–O bond cleavage: a new strategy for molecular diversity. *Chem. Soc. Rev.* **2014**, *43*, 8081−8097.

47. Somerville, R. J.; Hale, L. V. A.; Gómez-Bengoa, E.; Burés, J.; Martin, R. Intermediacy of Ni−Ni Species in sp^2 C−O Bond Cleavage of Aryl Esters: Relevance in Catalytic C−Si Bond Formation. *J. Am. Chem. Soc.* **2018**, *140*, 8771−8780.

48. Cordova, M.; Wodrich, M. D.; Meyer, B.; Sawatlon, B. Corminboeuf, C. Data-Driven Advancement of Homogeneous Nickel Catalyst Activity for Aryl Ether Cleavage. *ACS Catal.* **2020**, *10*, 7021−7031.

49. Schwarzer, M. C.; Konno, R.; Jojo, T.; Ohtsuki, A.; Nakamura, K.; Yasutome, A.; Takahashi, H.; Shimasaki, T.; Tobisu, M.; Chatani, N.; Mori, S. Combined Theoretical and Experimental Studies of Nickel-Catalyzed Cross-Coupling of Methoxyarenes with Arylboronic Esters via C−O Bond Cleavage. *J. Am. Chem. Soc.* **2017**, *139*, 10347−10358.

50. Jain, P.; Pal, S.; Avasare, V. $Ni(COD)_2$-Catalyzed *ipso*-Silylation of 2-Methoxynaphthalene: A Density Functional Theory Study. *Organometallics* **2018**, *37*, 1141−1149.

51. Xu, L.; Chung, L. W.; Wu, Y-D. Mechanism of Ni-NHC Catalyzed Hydrogenolysis of Aryl Ethers: Roles of the Excess Base. *ACS Catal.* **2016**, *6*, 483−493.

52. Wititsuwannakul, T.; Tantirungrotechai, Y.; Surawatanawong, P. Density Functional Study of Nickel N-Heterocyclic Carbene Catalyzed C−O Bond Hydrogenolysis of Methyl Phenyl Ether: The Concerted β-H Transfer Mechanism. *ACS Catal.* **2016**, *6*, 1477−1486.

53. Li, X.; Hong, X. Computational studies on Ni-catalyzed C-O bond activation of esters. *J. Organomet. Chem.* **2018**, *864*, 68−80.

54. Zhang, S-Q.; Hong, X. Mechanism and Selectivity Control in Ni- and Pd-Catalyzed Cross-Couplings Involving Carbon−Oxygen Bond Activation. *Acc. Chem. Res.* **2021**, *54*, 2158−2171.

55. Postils, V.; Delgado-Alonso, C.; Luis, J. M.; Salvador, P. An Objective Alternative to IUPAC's Approach To Assign Oxidation States. *Angew. Chem., Int. Ed.* **2018**, *57*, 10525−10529.

56. Kozuch, S. A refinement of everyday thinking: the energetic span model for kinetic assessment of catalytic cycles. *WIREs Computational Molecular Science* **2012**, *2*, 795−815.

57. Kozuch, S.; Shaik, S. How to Conceptualize Catalytic Cycles? The Energetic Span Model. *Acc. Chem. Res.* **2011**, *44*, 101−110.

58. Campbell, C. T. The Degree of Rate Control: A Powerful Tool for Catalysis Research *ACS Catal.* **2017**, *7*, 2770−2779.

59. Frisch, M. J.; Trucks, G. W.; Schlegel, H. B.; Scuseria, G. E.; Robb, M. A.; Cheeseman, J. R.; Scalmani, G.; Barone, V.; Petersson, G. A.; Nakatsuji, H.; Li, X.; Caricato, M.; Marenich, A. V.; Bloino, J.; Janesko, B. G.; Gomperts, R.; Mennucci, B.; Hratchian, H. P.; Ortiz, J. V.; Izmaylov, A. F.; Sonnenberg, J. L.; Williams-Young, D.; Ding, F.; Lipparini, F.; Egidi, F.; Goings, J.; Peng, B.; Petrone, A.; Henderson, T.; Ranasinghe, D.; Zakrzewski, V. G.; Gao, J.; Rega, N.; Zheng, G.; Liang, W.; Hada, M.; Ehara, M.; Toyota, K.; Fukuda, R.; Hasegawa, J.; Ishida, M.; Nakajima, T.; Honda, Y.; Kitao, O.; Nakai, H.; Vreven, T.; Throssell, K.; Montgomery, Jr., J. A.; Peralta, J. E.; Ogliaro, F.; Bearpark, M. J.; Heyd, J. J.; Brothers, E. N.; Kudin, K. N.; Staroverov, V. N.; Keith, T. A.; Kobayashi, R.; Normand, J.; Raghavachari, K.; Rendell, A. P.; Burant, J. C.; Iyengar, S. S.; Tomasi, J.; Cossi, M.; Millam, J. M.; Klene, M.; Adamo, C.; Cammi, R.; Ochterski, J. W.; Martin,

R. L.; Morokuma, K.; Farkas, O.; Foresman, J. B.; Fox, D. J. Gaussian 16, revision B.01; Gaussian, Inc.: Wallingford CT, 2016.

60. Zhao, Y.; Truhlar, D. G. The M06 suite of density functionals for main group thermochemistry, thermochemical kinetics, noncovalent interactions, excited states, and transition elements: two new functionals and systematic testing of four M06-class functionals and 12 other functionals. *Theor. Chem. Acc.* **2008**, *120*, 215−241.

61. Hay, P. J.; Wadt, W. R. Ab initio effective core potentials for molecular calculations. Potentials for K to Au including the outermost core orbitals. *J. Chem. Phys.* **1985**, *82*, 299−310.

62. Weigend, F.; Ahlrichs, R. Balanced basis sets of split valence, triple zeta valence and quadruple zeta valence quality for H to Rn: Design and assessment of accuracy. *Phys. Chem. Chem. Phys.* **2005**, *7*, 3297−3305.

63. Fukui, K. The path of chemical reactions - the IRC approach. *Acc. Chem. Res.* **1981**, *14*, 363−368.

64. Tomasi, J.; Mennucci, B.; Cammi, R. Quantum Mechanical Continuum Solvation Models. *Chem. Rev.* **2005**, *105*, 2999−3094.

65. Neese, F. The ORCA program system. *WIREs Comput. Mol. Sci.* **2022**, 12, e1491.

TOC graphic